Contents lists available at ScienceDirect

Transactions of Nonferrous Metals Society of China

36(2026) 96−111

www.tnmsc.cn

# 3D morphological characteristics of shrinkage porosities and their relationship with microstructures in Mg−12Al magnesium alloy

Chuang-ming LI [a,b,c], Ang ZHANG [a,b,c,*], Yong-feng LI [a,b,c], Heng-rui HU [a,b,c], He LIU [a,b,c], Yu-yang GAO [a,b,c], Zhi-hua DONG [a,b,c], Bin JIANG [a,b,c,**], Fu-sheng PAN [a,c]

[a] National Engineering Research Center for Magnesium Alloys, Chongqing University, Chongqing 400044, China;
[b] National Key Laboratory of Advanced Casting Technologies, Chongqing University, Chongqing 400044, China;
[c] College of Materials Science and Engineering, Chongqing University, Chongqing 400044, China

**Abstract:** The dependence of shrinkage porosities on microstructure characteristics of Mg−12Al alloy was investigated. The distribution, morphology, size, and number density of shrinkage porosities were analyzed under different cooling rates. The relationship between shrinkage porosities and microstructure characteristics was discussed in terms of temperature conditions, feeding channel characteristics, and feeding capacity. Further, the feeding behavior of the residual liquid phase in the solid skeleton was quantified by introducing permeability. Results show a strong correlation between the solid microstructure skeleton and shrinkage porosity characteristics. An increase in permeability corresponds to a declining number density of shrinkage porosities. This study aims to provide a more complete understanding how to reduce shrinkage porosities by controlling microstructure characteristics.

**Keywords:** Mg−12Al alloy; shrinkage porosity; solidification; microstructure characteristics; morphological characteristics

## 1 Introduction

Magnesium alloys are the lightest metallic structural materials with high specific strength, excellent shock absorption, good electromagnetic shielding, and high thermal conductivity [1−6]. The distinctive advantages lead to extensive applications in various fields, such as automotive, aerospace, electronics, and medical devices [3,7−13]. The cast Mg alloys, as major categories of Mg alloys, are formed by smelting and solidification. Because of the broad solidification temperature range and resultant mushy solidification behavior, the pores formed due to volume contraction are difficult to feed in most cast Mg alloys [14]. Once not fully fed by the liquid, the pores will become shrinkage porosities, one of the most common defects in the castings [15−18], which largely deteriorate mechanical properties, e.g., causing the stress concentration and accelerating the crack initiation and propagation [16,19−24].

The formation of shrinkage porosities involves metal flow, heat transfer, and phase transformation, which are closely related to solidification processes and casting conditions [25]. To reduce and eliminate shrinkage porosity, a large number of studies have been conducted to establish the relationship between casting conditions and shrinkage porosity features. LEE et al [26] compared the influence of the gate speed, intensification pressure, and melt temperature on

**Corresponding author:** *Ang ZHANG, Tel: +86-18811328068, E-mail: angzhang@cqu.edu.cn;
**Bin JIANG, Tel: +86-23-65102821, E-mail: jiangbinrong@cqu.edu.cn
https://doi.org/10.1016/S1003-6326(25)66951-2
Received 7 May 2024; accepted 10 January 2025

porosity distribution in high-pressure die-cast AM50 alloys. MI et al [27] simulated the low-pressure die-casting of wheel hubs and found that the rim−spoke connection is susceptible to shrinkage porosities, whereas adding the cooling system can effectively reduce shrinkage porosities. ZHANG et al [28] investigated the effects of vertical centrifugal casting parameters on shrinkage porosities in basin-shaped castings and found that the mold preheating temperature is the most significant parameter. LEE et al [29] studied the effects of process parameters on shrinkage porosities in high-pressure die casting, providing a correlation between process parameters and shrinkage porosities for a given geometry. LI et al [30] found that the porosities exist in thick walls and thick-thin wall junctions of cylinder heads, suggesting that regular shapes and thin walls are advantageous for reducing porosities.

These studies focus on optimizing process parameters and casting geometry to reduce shrinkage porosities, i.e., remaining on a macro level. The formation of shrinkage porosities is directly related to micro-feeding capacity in the solid microstructure skeleton. However, the relationship between the porosity-forming process and microstructure characteristics is not clear. Even the commonly used prediction criteria, e.g., the Niyama criterion [31] and the dimensionless Niyama criterion [32], mainly stress the macro process conditions, e.g., temperature gradient and cooling rate. The microstructure characteristics involve the growth of $\alpha$-Mg grains, the change in grain characteristics, and the precipitation of secondary phases, all of which affect the formation of shrinkage porosities. Accordingly, the formation tendency of shrinkage porosities cannot be simply assessed based on casting process parameters. Understanding the relationship between shrinkage porosities and microstructure characteristics is crucial for predicting and controlling shrinkage porosities.

The liquid is transformed into primary grains from nucleation sites once solidification starts. These grains grow and touch each other, forming a continuous solid skeleton. The remaining un-solidified liquid flows around these grains to feed the contraction of both solid and liquid phases. Whether the liquid feeding is sufficient directly impacts the formation of shrinkage porosities. Such feeding behavior is influenced by the tortuosity and width of the flow channels, and these two features are closely related to grain morphology and solid fraction. Accordingly, elucidating the effects of the distribution, morphology, and size of solid microstructures, including primary $\alpha$-Mg phases and secondary phases, can guide the control of shrinkage porosities.

The objective of this work is to reveal the effects of the microstructure characteristics on shrinkage porosities. Same-sized crucibles are used to remelt homogeneous alloys, and varying cooling methods are employed to obtain distinct microstructure characteristics. The distribution, morphology, size, and number density of shrinkage porosities are investigated, and the relationship to the feeding behavior of the residual liquid phase at late solidification is evaluated. By dissecting the formation tendency of shrinkage porosities, this work aims to develop a more comprehensive understanding how to reduce shrinkage porosities through microstructure control.

## 2 Experimental

### 2.1 Alloy material

As one of the earliest developed and most widely used Mg alloys, the Mg−Al alloy system has good formability, excellent mechanical properties, and high corrosion resistance. However, the broad solidification temperature range makes Mg−Al alloys more prone to forming shrinkage porosity defects. Taking the Mg−10Al (wt.%) alloy for example, the solidification ranges under the equilibrium and Scheil non-equilibrium solidification conditions are 127 ℃ and 161 ℃, respectively.

According to the Mg−Al binary equilibrium phase diagram, the maximum solubility of Al in Mg is around 12%, which corresponds to the peak of the equilibrium solidification range. Thus, this study focused on investigating the Mg−12Al (wt.%) alloy, and the findings would have broader implications for Mg alloys overall.

### 2.2 Casting process

Pure Mg and Al alloys were used to prepare the Mg−12Al alloy. The preheating temperatures of both the master alloys and the mild steel crucible were 200 °C. The master alloys were heated to

730 °C and held for 10 min under a protective gas mixture of $CO_2$ + $SF_6$ (with a volume ratio of 99:1). After coating a thin layer of hexagonal boron nitride inside the mold and preheating at 300 °C for 10 min, the melt was poured into a permanent casting mold.

The chemical composition of the alloy was determined using an Optima 8000 inductively coupled plasma optical emission spectrometer (ICP-OES). The measured Al content in the alloy was 12.49 wt.%, closely matching the nominal design composition.

Three sets of cylindrical specimens, each with a diameter of 80 mm and a height of 130 mm, were processed from the ingots. These specimens were placed in a mild steel crucible with a diameter of 88 mm and a height of 260 mm. Placed in a duplex-stage quenching furnace (as illustrated in Fig. 1(a)), the cylindrical specimens underwent remelting in a protective gas environment. This furnace offered three levels of cooling. First, once the cylindrical specimens melted in the melting chamber, the power supply was cut off, and the furnace cover was opened, facilitating first-level cooling. These specimens are denoted as F# (furnace cooling). Second, specimens were moved to the slow-cooling chamber with a base-moving rod, labeled A# (air cooling). Lastly, specimens dropped into the rapid cooling chamber filled with a cooling medium, labeled W# (water cooling). During solidification, three K-type thermocouples with a 1 mm diameter were inserted into the molten metal, positioned 40 mm above the melt bottom, and spaced 20 mm apart, sequentially named thermocouple 1, thermocouple 2, and thermocouple 3 (as illustrated in Fig. 1(b)). Thermocouple 1 aligned precisely with the axis of the cylindrical crucible. These three thermocouples were linked to a temperature collector, which recorded the temperature−time curve of the molten metal at a frequency of 10 Hz during solidification.

### 2.3 Characterization

The microstructure characteristics and shrinkage porosities adjacent to thermocouple 2 were examined and characterized. The specimens were ground using SiC paper with grits of 120−1200 and then polished with diamond paste down to a size of 0.25 μm. After cleaning in an ultrasonic ethanol bath, the specimens were then etched with a 3% Nital solution (consisting of 97 mL ethanol and 3 mL nitric acid). The microstructure was analyzed using a scanning electron microscope (SEM, JEOL JSM−7800F). The electron backscatter diffraction (EBSD; HKL Channel 5 System equipped with an FEI Nova 400 FEG-SEM, Cambridge, MA) analysis was performed, with a step size of 5 μm. For EBSD observation, the specimens were electrolytically polished in the AC2 solution at −30 °C and 20 V for 90 s.

Cylindrical specimens, each 4 mm in diameter and 6 mm in length were extracted near the thermocouple 2 and prepared for micro-computed tomography (Micro-CT) scanning. Scanning and analysis of shrinkage porosities were conducted by a BRUKER SKYSCAN 1276 micro-computed tomography inspection device. Operating voltage

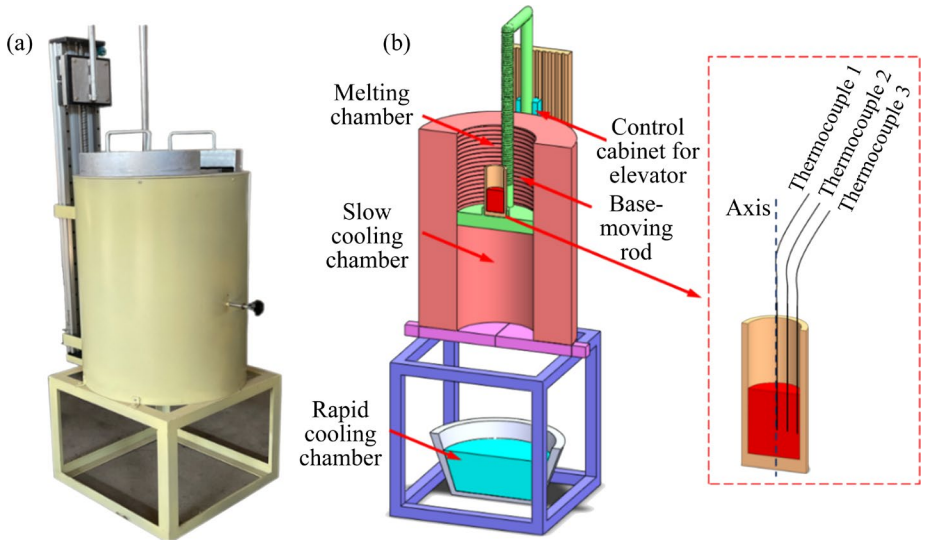


**Fig. 1** (a) Physical and (b) schematic diagrams of duplex-stage quenching furnace

and current of the device were set to be 100 kV and 200 μA, respectively. The resolution of a pixel was 4 μm. The scanned results of the alloy specimens were reconstructed and analyzed using CT-Analyser v1.2.0, CT-Volume v2.3.2, and DataViewer v1.7.0 software.

### 2.4 Morphological parameters

A quantitative analysis of shrinkage porosities was achieved by introducing the morphological parameters. $S_{ph}$ refers to the ratio of the surface area of a sphere that has the same volume as the shrinkage porosity to the actual surface area of the shrinkage porosity:

$$S_{ph}=\pi D_{V\text{-}eq}^2/S_A \quad (1)$$

where $S_A$ represents the actual surface area of the shrinkage porosity, μm$^2$; $D_{V\text{-}eq}$ is the diameter of the sphere with the same volume as the shrinkage porosity, μm. These parameters were obtained using CT-Analyser v1.2.0 software.

$S_{ph}$ is a dimensionless parameter ranging from 0 to 1, with smaller values indicating more irregular shrinkage porosity. If the morphological parameter exceeds a threshold, the pore shape becomes regular and another common type of pore defect, gas porosity, appears. Considering the morphological distinctions between gas porosity and shrinkage porosity [18,33−35], the pore defects with $S_{ph}$<0.60 were analyzed in the present work.

To quantify the morphological complexity of the solid skeleton (i.e., α-Mg phase), the fractal dimension ($F_d$), a non-integer dimension, was introduced to characterize the complexity and irregularity of the skeleton shape. The concept of fractals was proposed in the 1970s by the French mathematician Mandelbrot, who aimed to describe shapes or curves that the traditional Euclidean geometry could not describe [36,37]. In the field of metal materials, the fractal theory is used extensively to quantify various microstructural morphologies, such as dislocation patterns [38], fracture surfaces [39], grain boundaries [40], martensitic phase transformations [41], segregation morphologies [42], and dendritic structures [43−47]. $F_d$ can be used to describe the relative intricacy of a given figure. For a 2D image, $F_d$ ranges between 1 and 2. A value closer to 1 indicates a smoother 2D figure, while a value closer to 2 suggests more complexity. The prevalent methods to calculate $F_d$ are the box-counting method and the perimeter-area method. In this study, the box-counting method was employed, and the calculating process is illustrated in Fig. 2. By varying the box size ($r$), the number of boxes $N(r)$ covering the target microstructure was calculated for different $r$ values. The fractal dimension of the target microstructure can be determined using Eq. (2):

$$N(r)=r^{-F_d}\cdot c \quad (2)$$

where $c$ is a constant.

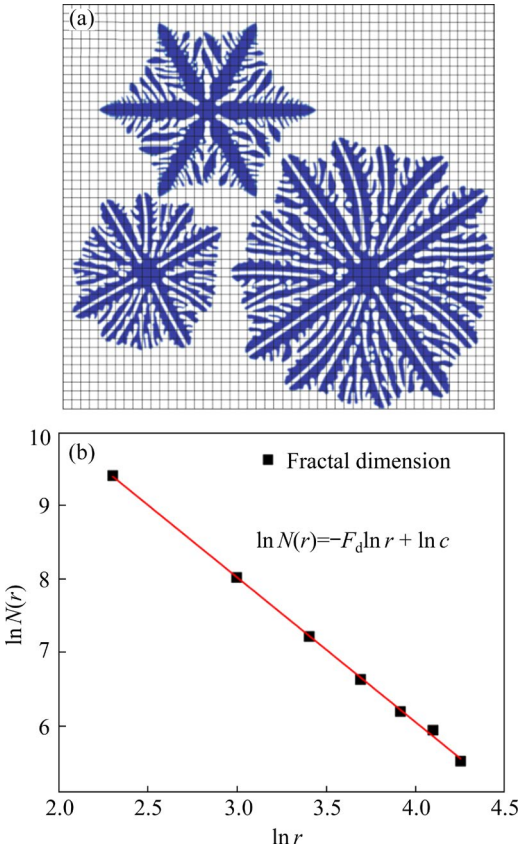


**Fig. 2** Schematic diagram for calculating fractal dimension of target microstructure by box-counting method: (a) Box grid overlaid on Mg microstructure; (b) Relation between ln $N(r)$ and ln $r$ ($r$ is the box size, and $N(r)$ is the number of boxes)

Using ln $r$ and ln $N(r)$ as the coordinates of the scatterplot, a linear fit is applied to the data points through the least square method. The absolute value of the slope of the fitted curve represents $F_d$.

## 3 Results

### 3.1 Solidification curves and microstructures

Figures 3(a−c) depict change of solidification

temperature versus time and instantaneous cooling rate curves of specimens W#, A#, and F#. The cooling rate is solved by the derivative of cooling temperature to time. The liquidus and solidus temperatures of the Mg−12Al alloy are also indicated. These temperatures are determined using the JmatPro solidification module, with an initial temperature of 700 °C and a step size of 0.01 °C. Specimen W# shows the shortest solidification time, i.e., 26 s from the liquidus temperature to solidus temperature, and the highest instantaneous cooling rate, i.e., 5.769 °C/s. The average cooling rate of specimen W# is 21.2 times that of specimen A# (0.272 °C/s), while the average cooling rate of specimen A# is 3.1 times that of specimen F# (0.089 °C/s). Therefore, specimens W#, A#, and F# undergo significantly different cooling conditions during the solidification stage.

Figures 3(d−f) show the microstructures of specimens W#, A#, and F# under different cooling conditions. In specimen W#, $\alpha$-Mg and the secondary phase show a fine and dispersed distribution. With the decrease in the average cooling rate, the alloy microstructure becomes coarser, and the sizes of $\alpha$-Mg and the secondary phase increase. The average grain sizes in specimens W#, A#, and F# are 127, 193, and 253 μm, respectively (Figs. 3(g−i)), demonstrating increasingly refined microstructures with the increase in the cooling rate.

The formation of shrinkage porosities has a close correlation with the microstructure characteristic. The change in the microstructures under different cooling rates indicates a different distribution of the shrinkage porosities among specimens W#, A#, and F#.

### 3.2 Distribution of shrinkage porosities

Figure 4 shows the distribution of shrinkage porosities in both vertical (Figs. 4(a−c)) and horizontal (Figs. 4(d−f)) directions in specimens W#, A#, and F#. The shrinkage porosities in specimen W# are the smallest. As the cooling rate decreases (from specimen W# to specimen F#), the

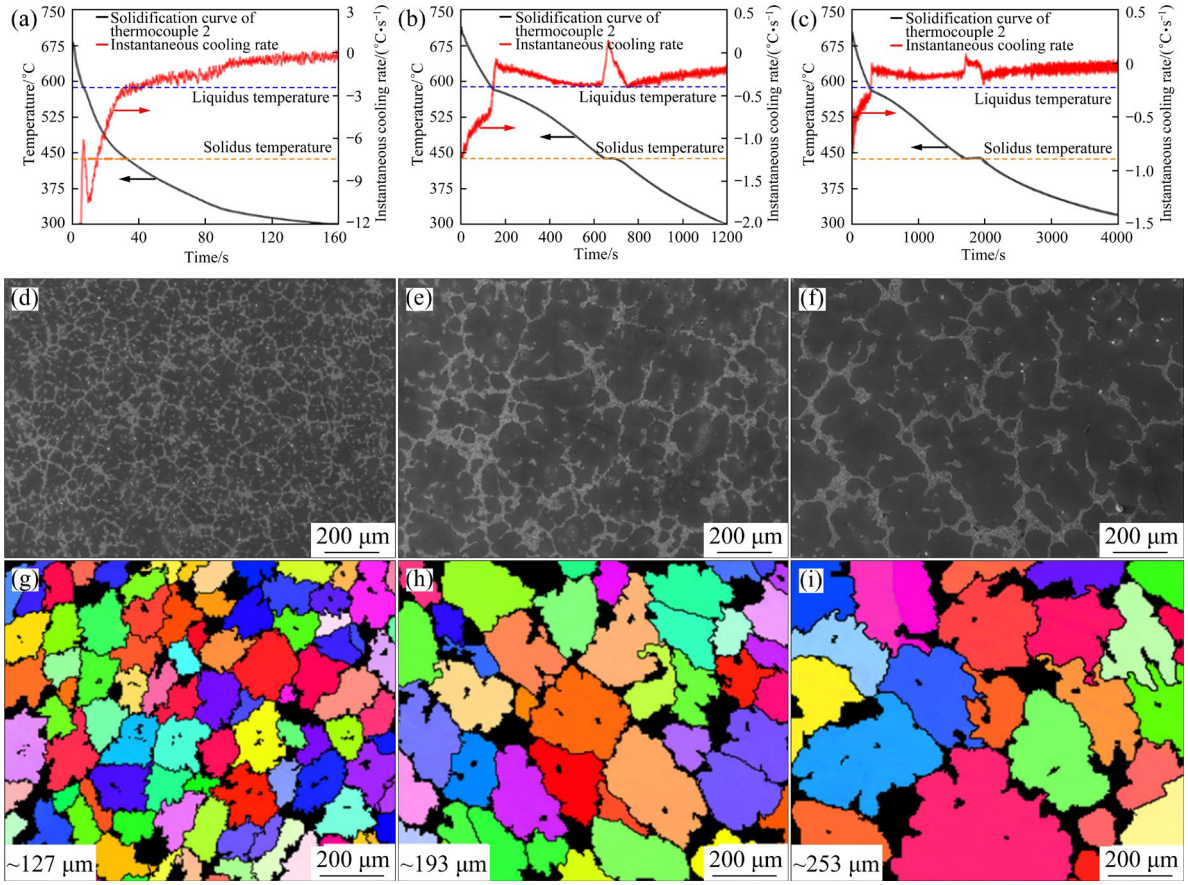


**Fig. 3** Solidification curves and microstructures in different specimens: (a−c) Solidification curves of specimens W#, A#, and F#, respectively; (d−f) SEM microstructures of specimens W#, A#, and F#, respectively; (g−i) EBSD results of specimens W#, A#, and F#, respectively

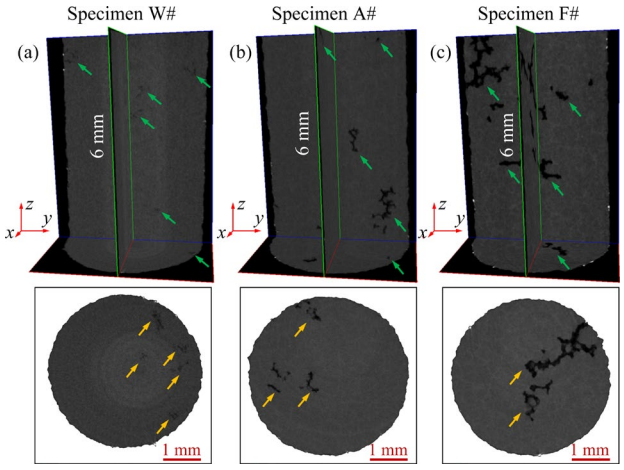


**Fig. 4** 2D photos of specimens W#, A# and F#: (a−c) Longitudinal slices; (d−f) Horizontal slices

size of shrinkage porosities increases.

For clearer observation of the distribution of shrinkage porosities, the two-dimensional shrinkage porosities are examined, as shown in Fig. 5. With the decrease of the average cooling rate, the number of the shrinkage porosities presents an opposite trend to the change in the size of shrinkage porosities. Specimen W# displays the highest number density but the smallest size of shrinkage porosities (as depicted in Figs. 5(a−c)).

The three-dimensional distribution of the shrinkage porosities is similar to the 2D results. Figure 6 illustrates the micro-CT scan results of the Mg−12Al alloy. Each alloy is tested on two sets of specimens, designated as W1#, W2#, A1#, A2#,

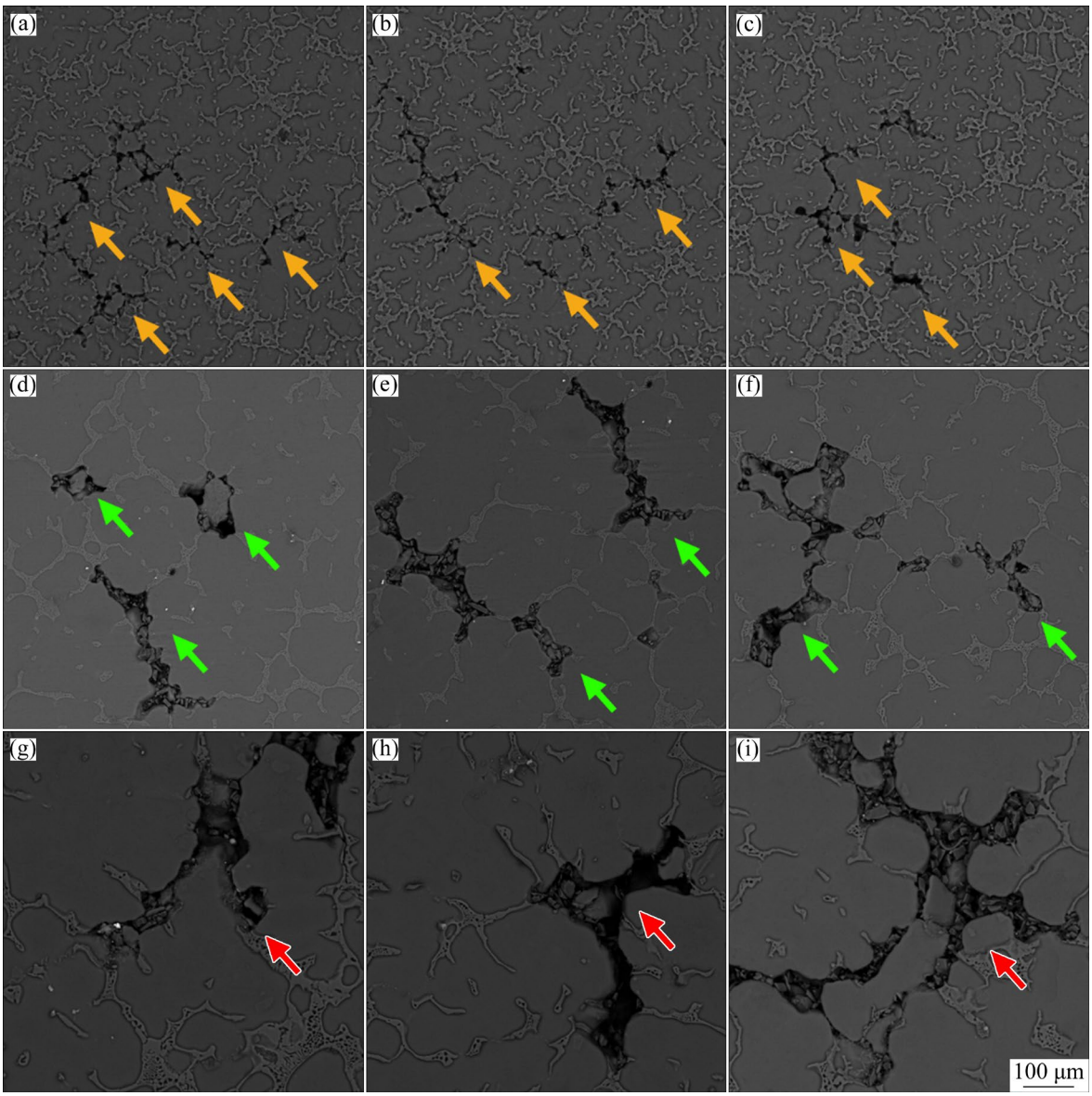


**Fig. 5** Two-dimensional distribution of shrinkage porosities in different specimens: (a−c) Specimen W#; (d−f) Specimen A#; (g−i) Specimen F#

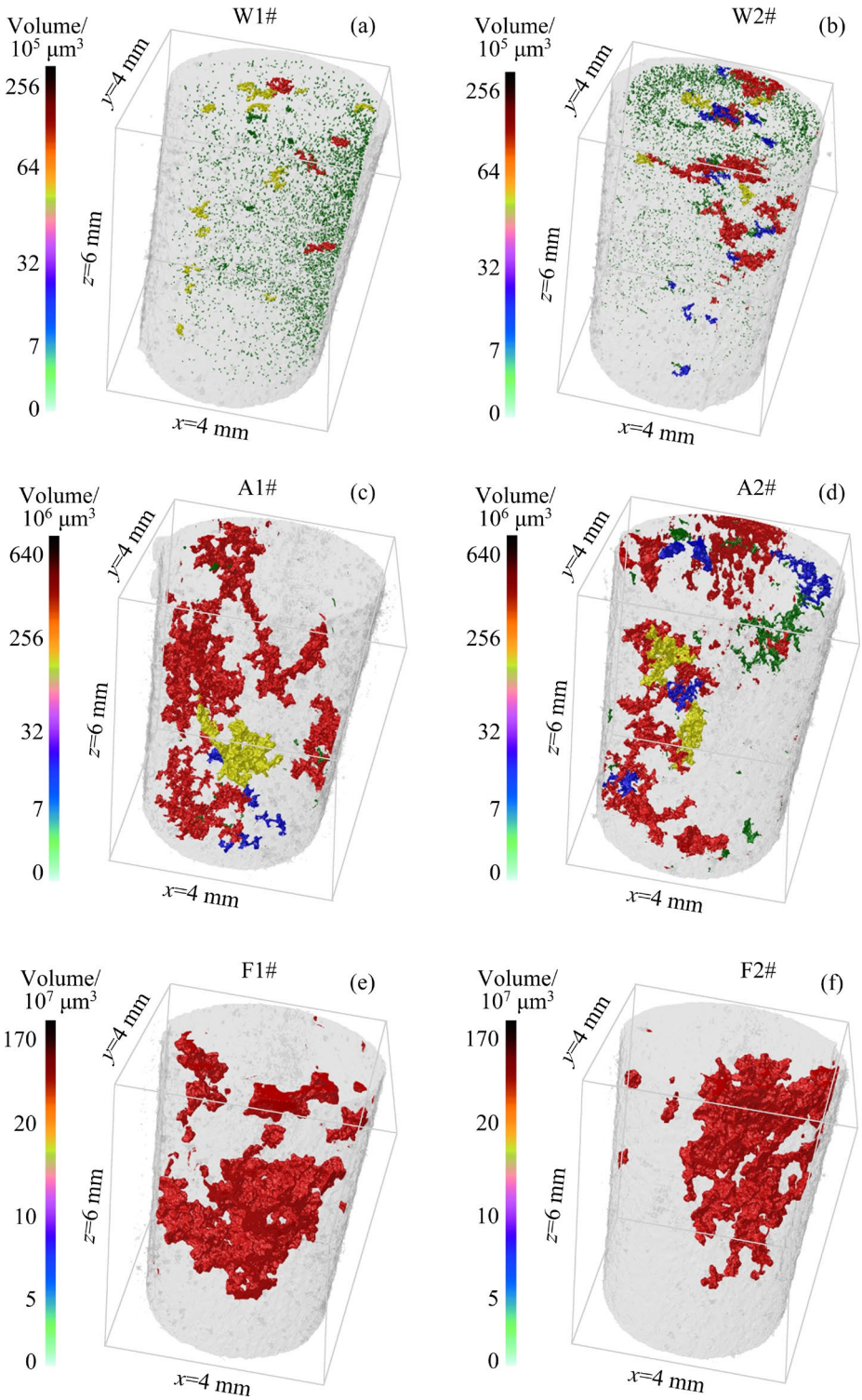


**Fig. 6** Micro-CT scan results of shrinkage porosities in different specimens: (a, b) Specimen W#; (c, d) Specimen A#; (e, f) Specimen F#

F1#, and F2#. Significant variations in porosity distribution are found in different specimens. In specimen F#, the size of shrinkage porosities is relatively large, resulting in a low density of shrinkage porosities. As the cooling rate increases, the size of shrinkage porosities decreases, while the density increases. Specimen W# displays the highest density of the shrinkage porosities, characterized by a dense distribution (as depicted in Figs. 6(a, b)). In specimen F#, the larger shrinkage porosities exhibit a continuous reticulate distribution pattern (as illustrated in Figs. 6(e, f)).

### 3.3 Morphology and size of shrinkage porosities

By generating data subsets for individual shrinkage porosities, the three-dimensional characteristics can be quantified and visualized. Figure 7 displays the morphology of individual shrinkage porosities, with $S_{ph}$ and $D_v$ marked. $D_v$ represents the diameter of a sphere with a volume equivalent to the shrinkage porosity. In specimen W#, as depicted in Fig. 7(a), shrinkage porosities exhibit a "slimmer" morphology and higher morphological complexity (i.e., lower $S_{ph}$). In specimen A#, the size of shrinkage porosities increases, accompanied by reduced morphological complexity (as shown in Fig. 7(b)). With a further decrease in the average cooling rate, both $D_v$ and $S_{ph}$ increase, displaying larger size and lower complexity in morphology (Fig. 7(c)).

To analyze the size and morphology of shrinkage porosities, the relationship between $S_{ph}$ and $D_v$ is quantified. Figure 8(a) denotes that $S_{ph}$=0.23 and $D_v$=400 μm, respectively. $S_{ph}$ decreases as $D_v$ increases, indicating an inverse relationship between the two. Notably, shrinkage porosities with lower $S_{ph}$ are more likely to form in specimen W#, evidenced by their presence (indicated by the red arrows in Fig. 8(a)) primarily in specimen W#. As the cooling rate decreases, the trend of forming shrinkage porosities with low $S_{ph}$ in specimens A# and F# diminishes, reducing the morphological complexity of the shrinkage porosities. Shrinkage porosities with complex morphologies (i.e., lower $S_{ph}$) are more likely to

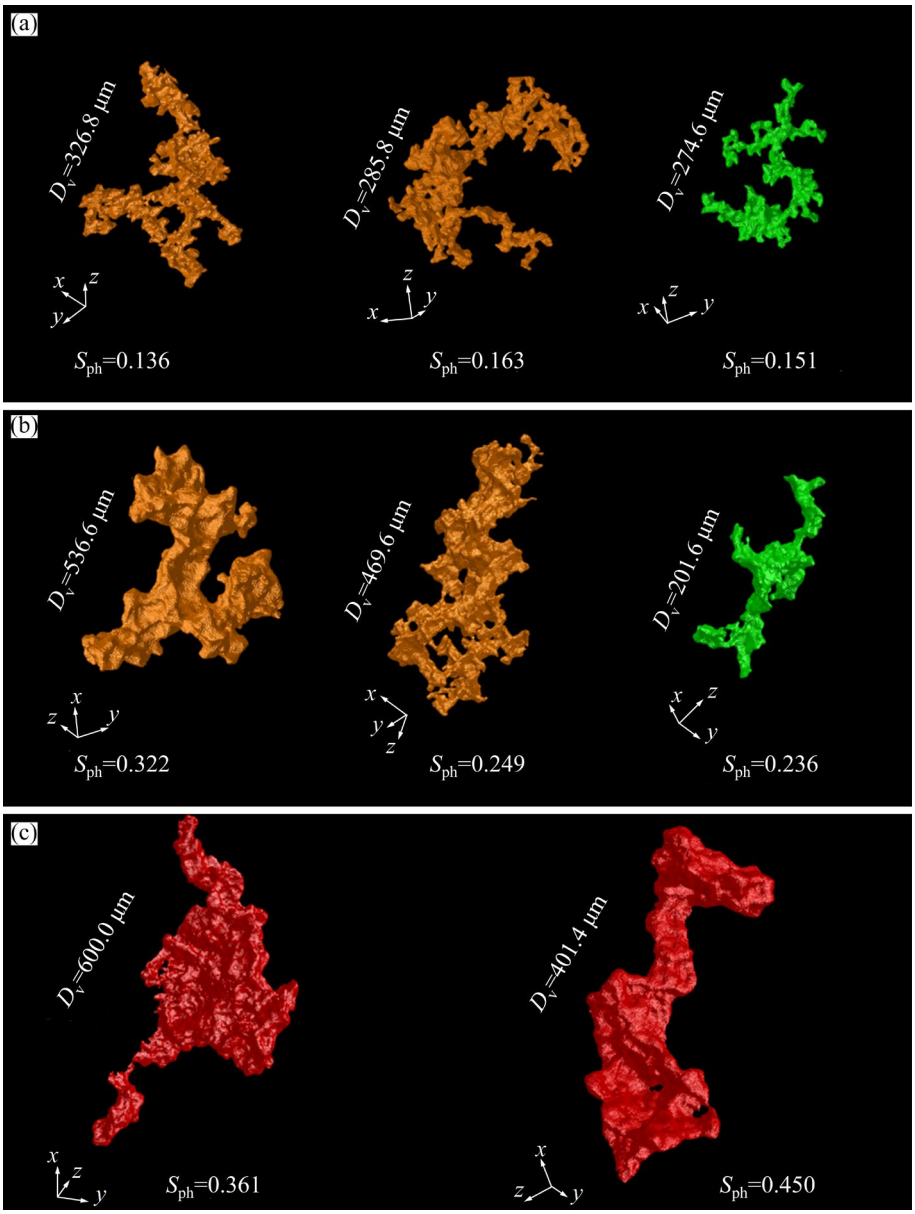


**Fig. 7** Morphology and size of individual shrinkage porosities: (a) Specimen W#; (b) Specimen A#; (c) Specimen F#

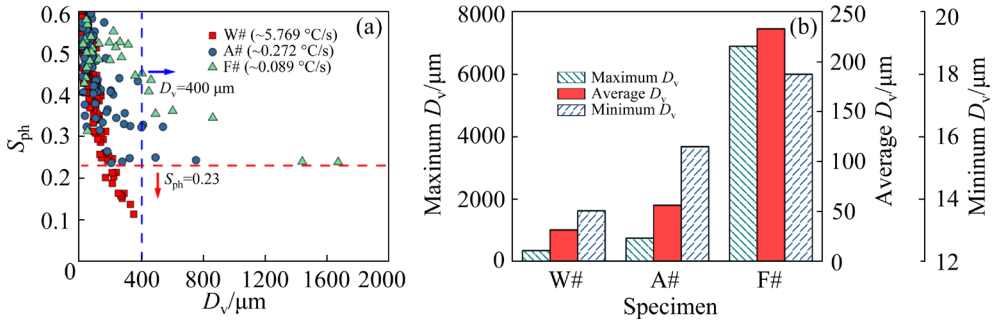


**Fig. 8** (a) Relationship between $D_v$ and $S_{ph}$ of shrinkage porosities in different specimens; (b) Change of $D_v$ of shrinkage porosities in different specimens

form in specimens with higher cooling rates.

In specimen W#, the shrinkage porosities generally have smaller sizes, and $D_v$ greater than 400 μm is mainly found in specimens A# and F#, as evidenced by their presence (indicated by the blue arrows in Fig. 8(a)). Figure 8(b) shows the change of the maximum size (maximum $D_v$), the average size (average $D_v$), and the minimum size (minimum $D_v$) of shrinkage porosities in specimens W#, A#, and F#. The average $D_v$ represents the mean value of $D_v$ for all shrinkage porosities within the specimens, characterizing the overall size of shrinkage porosities. The maximum, minimum, and average $D_v$ of shrinkage porosities all increase as the cooling rate decreases, indicating a strong dependence of the size of shrinkage porosities on the cooling rate.

### 3.4 Number density of shrinkage porosities

Figure 9 shows the distribution of the number density of shrinkage porosities in specimens W#, A#, and F#, with the side length of the cubes being 2 mm. For each specimen set (F#, A#, and W#), three cubes are used in the calculation of the number density of shrinkage porosities. Besides the change in the morphology and size, the number density of shrinkage porosities presents notable differences. As the cooling rate decreases, the number density decreases, and specimen W# shows the highest number density.

In summary, shrinkage porosities in specimen W# exhibit the smallest size, and the most complex morphology, but the highest number density, presenting a dense distribution feature. As the cooling rate decreases, there is a significant increase in the size of shrinkage porosities, a decrease in morphology complexity, and a reduction in the number density of the shrinkage porosities, corresponding to the formation of large-size network distribution patterns.

## 4 Discussion

A comparative analysis of the distribution, morphology, size, and number density of shrinkage porosities in specimens W#, A#, and F# was conducted. These characteristics undergo significant changes, which are closely linked to temperature conditions and microstructure characteristics. In this section, an analysis of the temperature conditions, together with a comparison with the Niyama criterion, is conducted, followed by the discussion of the feeding channels in the microstructure skeleton. The feeding behavior of the residual liquid phase at late solidification is further quantified to evaluate the formation tendency of shrinkage porosities.

### 4.1 Temperature conditions

Figures 10(a−c) illustrate the temperature difference ($\Delta T$) between thermocouple 1 and thermocouple 3, and the instantaneous cooling rate at thermocouple 2 in specimens W#, A#, and F#. $\Delta T$ decreases as the cooling rate decreases, and both $\Delta T$ and the cooling rate vary significantly among different specimens. The distance between thermocouple 1 and thermocouple 3 is 40 mm, and $\Delta T$ can be used to quantify the temperature gradients (the ratio of the temperature difference between two points to the distance between them). Therefore, the temperature gradient decreases as the cooling rate decreases, and specimen F# has the lowest temperature gradient.

The remarkable difference in the temperature

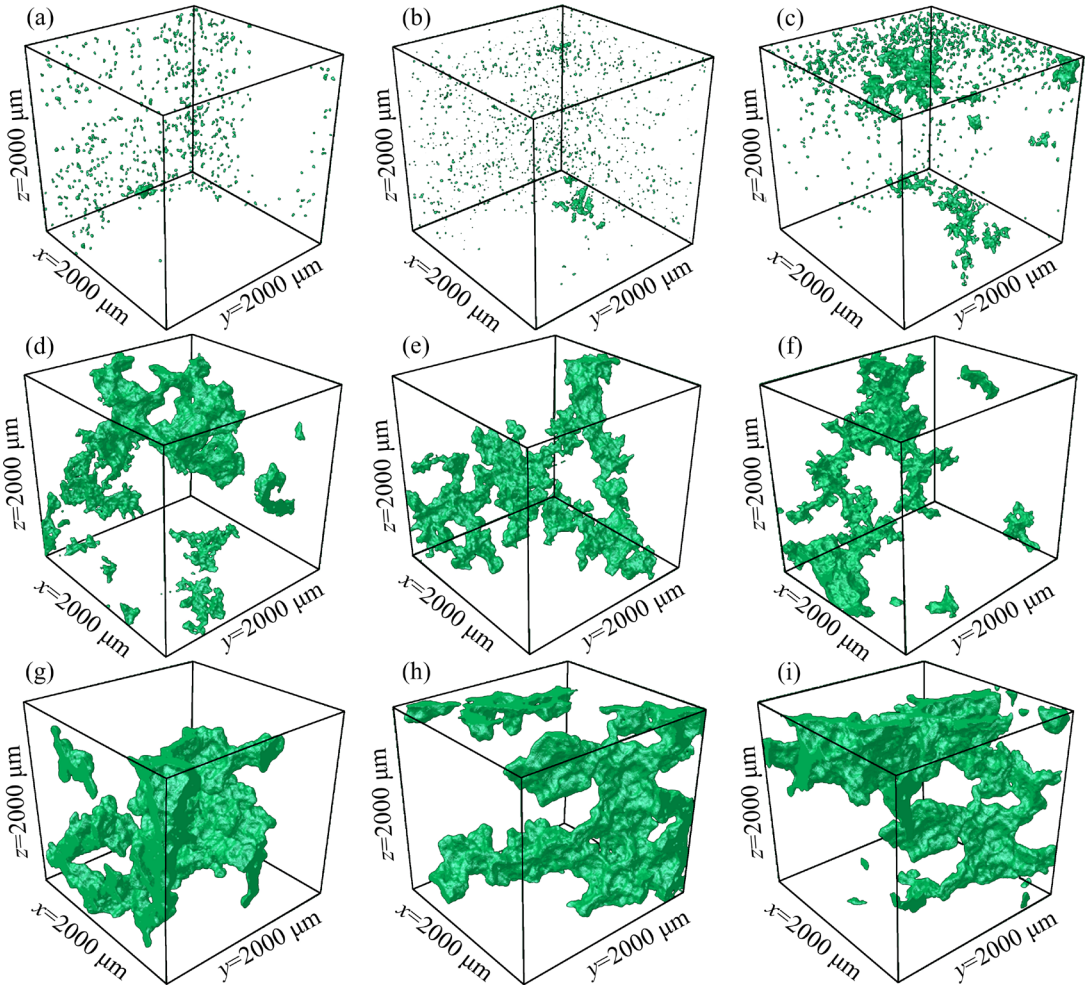


**Fig. 9** Number density of porosity porosities in different specimens: (a−c) Specimen W#; (d−f) Specimen A#; (g−i) Specimen F#

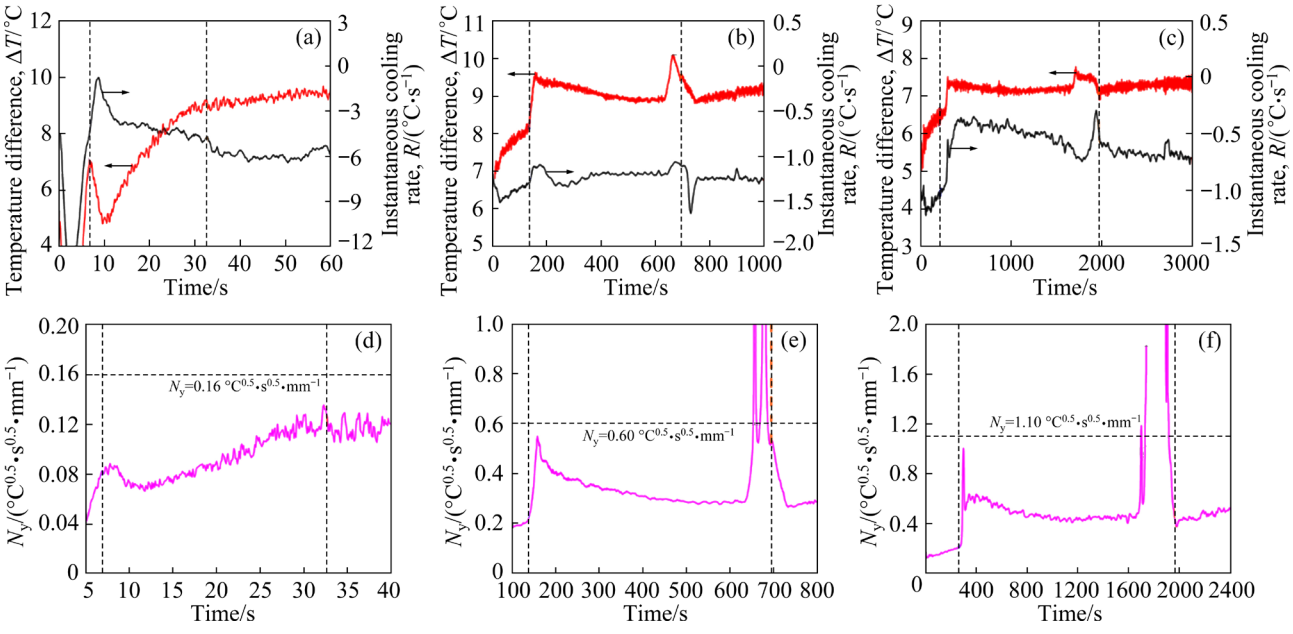


**Fig. 10** Temperature conditions and Niyama value ($N_y$) in different specimens: (a−c) Temperature difference and instantaneous cooling rate in specimens W#, A#, and F#, respectively; (d−f) $N_y$ at thermocouple 2 in specimens W#, A#, and F#, respectively

conditions indicates the presence of the porosity differences in different specimens. A classical pore prediction criterion, named the Niyama criterion [32], is first used to evaluate the effect of the temperature conditions:

$$N_y = G/\sqrt{R} \tag{3}$$

where $R$ represents the cooling rate, °C/s; $G$ denotes the temperature gradient, °C/mm. A smaller $N_y$ value indicates a greater formation tendency of shrinkage porosities [48].

The variation trend of $N_y$ values is illustrated in Figs. 10(d−f), where the cooling rate is measured at thermocouple 2, and the temperature gradient is calculated between thermocouple 1 and thermocouple 3. In the specimen W#, $N_y$ values are less than 0.16 $°C^{0.5}·s^{0.5}·mm^{-1}$. With decreasing the cooling rates, the $N_y$ values increase. $N_y$ values in the specimen A# generally remain below 0.60 $°C^{0.5}·s^{0.5}·mm^{-1}$, and in specimen F#, $N_y$ values are typically less than 1.10 $°C^{0.5}·s^{0.5}·mm^{-1}$.

Figures 11(a−c) illustrate the distribution of $N_y$ values in specimens W#, A#, and F#. In specimen W#, the $N_y$ values mainly range from 0.07 to 0.13 $°C^{0.5}·s^{0.5}·mm^{-1}$. As the cooling rate decreases, the distribution range narrows, but the values increase. Figure 11(d) illustrates the variation of the maximum, minimum, and average $N_y$ values. The average $N_y$ value increases with decreasing cooling rate, while the maximum and minimum $N_y$ values first increase and then decrease. Thus, specimen W# exhibits the lowest $N_y$ value during solidification.

According to the Niyama criterion, specimen W# has the greatest tendency to form shrinkage porosities due to the lowest $N_y$ values. However, the regions near thermocouple 2 in specimens A# and F# have more shrinkage porosities (see Fig. 6), indicating that the distribution of shrinkage porosities is not solely dependent on temperature conditions. As a macroscopic empirical prediction criterion, the Niyama criterion only considers the influence of temperature parameters on shrinkage porosities. This limitation indicates that exploring the dependence of shrinkage porosities on microstructure characteristics and liquid metal flow is of utmost need from a microscopic perspective.

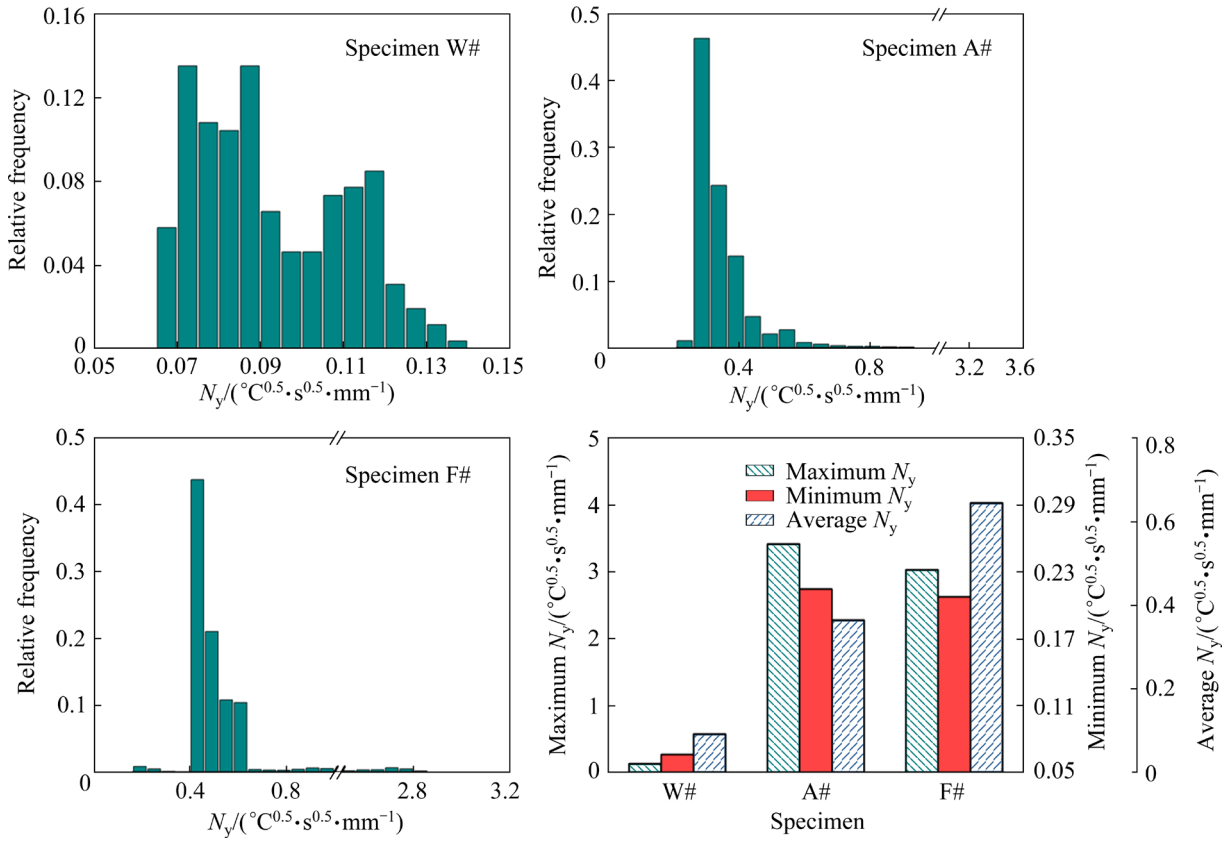


**Fig. 11** (a−c) Frequency distribution of $N_y$ values in different specimens; (d) Change of $N_y$ values in specimens W#, A# and F#

### 4.2 Feeding channel

The shrinkage porosities form at late solidification. At this stage, most of the melt is transformed into a solid phase, leaving a small fraction of the residual liquid phase within the solidifying solid skeleton. As the temperature drops, the residual liquid phase solidifies to form the secondary phase, and insufficient feeding within the $\alpha$-Mg skeleton leads to the formation of shrinkage porosities that coexist with the secondary phase.

Shrinkage porosities are influenced by the complexity of the feeding channel. Figure 12(a) depicts the change in $F_d$ of the $\alpha$-Mg solid skeleton. Decreasing cooling rates corresponds to a gradual reduction in $F_d$, meaning a simpler solid skeleton structure. In specimens W# with insufficient feeding, shrinkage porosities have complex morphologies, while in specimens F#, a lower solid skeleton complexity yields simpler porosity morphologies, as highlighted in the red dashed box in Fig. 12(a). The change in the $\alpha$-Mg skeleton complexity shows a close correlation with the $S_{ph}$ of the porosities (in Fig. 8(a)). As the cooling rates drop, the complexity of the $\alpha$-Mg solid skeleton decreases, leading to higher $S_{ph}$, i.e., simpler porosity morphologies.

The specific surface area ($S_v$), a measure of structure coarsening, quantifies the ratio of the perimeter to the area for a given 2D shape. A decreased $S_v$ indicates a coarser alloy structure. Figure 12(b) illustrates the change in $S_v$ in $\alpha$-Mg solid skeleton. $S_v$ decreases from specimen W# to A# and then to F#, indicating a coarsening solid skeleton. Figure 13 depicts the microstructure characteristics of different specimens after binarization (green for the $\alpha$-Mg phase and red for the secondary phase). Coarsening of the $\alpha$-Mg solid skeleton increases the width of feeding channels in the solid skeleton. Thus, alloys with wider feeding channels are more prone to form larger shrinkage porosities in areas with insufficient feeding.

Wider feeding channels result in larger shrinkage porosities in feeding-deficient area. Thus, in specimens W#, A#, and F#, decreasing cooling rates enlarge feeding channels, increasing the possibility of forming large shrinkage porosities. Notably, from W# to A# to F#, the $D_v$ of shrinkage porosities increases (as shown in Fig. 8(b)).

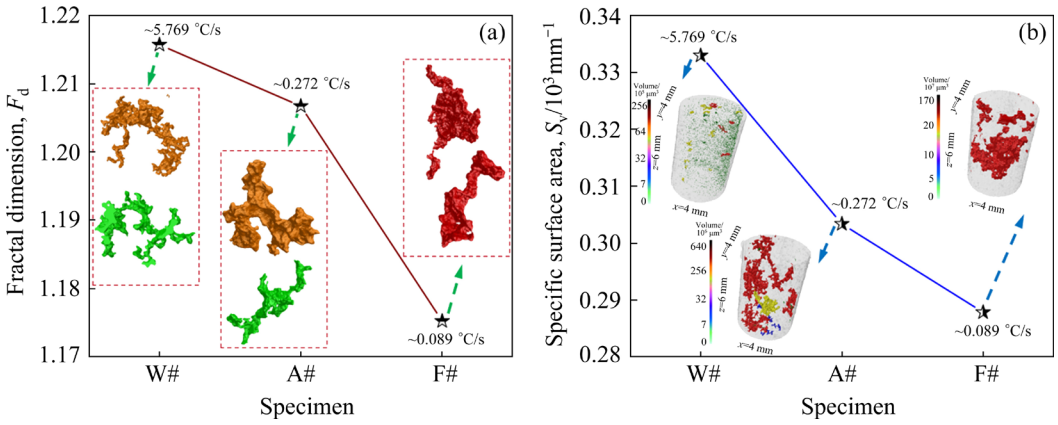


**Fig. 12** (a) Fractal dimension and (b) specific surface area of $\alpha$-Mg solid skeleton (i.e., feeding channel) in different specimens

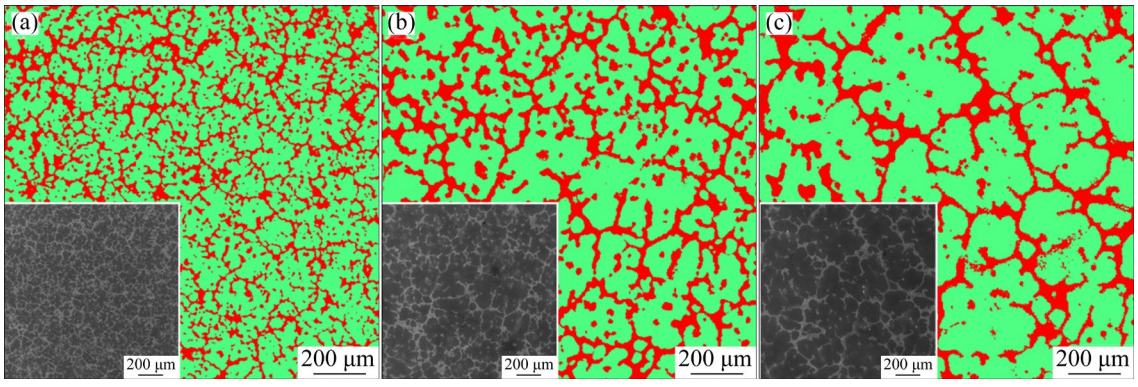


**Fig. 13** Microstructure characteristics of specimens after binarization: (a) W#; (b) A#; (c) F#

### 4.3 Feeding capacity

The feeding behavior of the residual liquid is chiefly influenced by solidified skeleton characteristics. A simple solidified skeleton enhances feeding efficiency, while a complex skeleton increases flow resistance due to tortuous feeding channels.

To quantify the feeding capacity, Darcy's Law is applied, where the liquid flow in the dendritic zone is transformed into a flow problem within a porous medium. The average flow velocity in the feeding channel can be described by Eq. (4):

$$v=\frac{KA\Delta P}{\mu_l L(1-g_s)} \tag{4}$$

where $\Delta P$ represents the pressure drop across the flow channel, Pa; $v$ indicates the average fluid velocity, m/s; $A$ represents the cross-sectional area perpendicular to the flow direction, $m^2$; $L$ denotes the length of the flow channel, mm; $\mu_l$ stands for the dynamic viscosity of liquid metal, Pa·s; $g_s$ represents the solid fraction in the mushy zone; $K$ is the permeability, which describes the fluid flow within the porous medium and plays a crucial role in influencing the feeding behavior of the liquid metal in the mushy zone.

Derived from Poiseuille's equation, the Carman−Kozeny equation is used to calculate the permeability $K$:

$$K=\frac{(1-g_s)^3}{k_c S_v^2 g_s^2} \tag{5}$$

where $k_c$ is a constant, defined as $k_c=k_0\tau$ ($k_0$ is a constant ranging between 2 and 3, and $\tau$ represents tortuosity quantified by the fractal dimension [44,49]). $\tau$ depicts the non-straightness of the feeding channel, which is mainly affected by the morphology of the solidified skeleton. Table 1 lists the parameter values used to calculate the permeability in different specimens.

Figure 14(a) shows permeability calculations of the intergranular liquid phase within the $\alpha$-Mg solid skeletons. The feeding capacity of the residual liquid phase increases as the cooling rate decreases. In Fig. 14(b), the number density in specimen W# exhibits 9.04 times that in specimen A#, and the number density in specimen A# is 1.76 times that of specimen F#, suggesting increasing density with cooling rate. Hence, reducing the feeding capacity of the liquid phase results in more deficient feeding areas and a higher number density of the shrinkage porosities.

**Table 1** $F_d$, $S_v$, $g_s$, and $k_0$ used to calculate permeability in specimens W#, A#, and F#

| Specimen | $F_d$ | $S_v$/mm$^{-1}$ | $g_s$ | $k_0$ |
|---|---|---|---|---|
| W# | 1.211 | 327.9 | 0.829 | 2.5 |
| A# | 1.201 | 298.3 | 0.830 | 2.5 |
| F# | 1.170 | 282.8 | 0.836 | 2.5 |

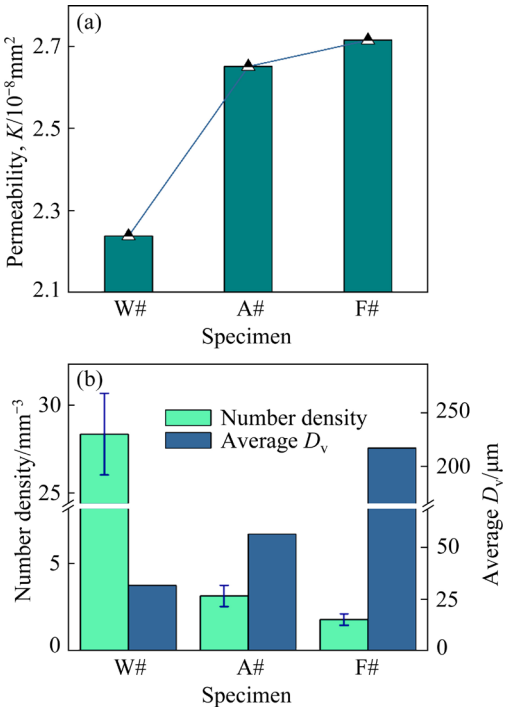


**Fig. 14** (a) Permeability in different specimens; (b) Number density and average $D_v$ of shrinkage porosities in different specimens

The volume fraction of shrinkage porosities in the alloy is primarily influenced by two factors: number density and average $D_v$. The latter, as mentioned earlier, increases with the widening of feeding channels (as shown in Fig. 14(b)). However, the width of the feeding channel also affects the feeding capacity of the residual liquid phase, which, in turn, affects the number density of shrinkage porosities. Accordingly, the number density and average $D_v$ of shrinkage porosities are strongly interrelated and jointly determine the volume fraction of shrinkage porosities.

## 5 Conclusions

(1) As the cooling rates decrease, distribution

of shrinkage porosities changes from dense to a large-size net, the porosity size increases, the morphological complexity weakens, and the number density decreases significantly.

(2) As the cooling rates decrease, notable changes occur in the solid-phase skeleton, consistent with the change in shrinkage porosities. With decreasing cooling rates, widening solid skeleton increases porosity size, and the reduced solid complexity decreases the tendency to form shrinkage porosities with complex morphologies.

(3) Permeability in alloy castings exhibits a strong correlation with the number density of shrinkage porosities. The reduced feeding capacity within the solid skeleton increases liquid flow resistance, causing insufficient feeding and a higher number density.

## CRediT authorship contribution statement

**Chuang-ming LI:** Conceptualization, Data curation, Formal analysis, Investigation, Methodology, Validation, Writing – Original draft; **Ang ZHANG:** Funding acquisition, Investigation, Methodology, Project administration, Resources, Software, Supervision, Validation, Visualization, Writing – Original draft, Writing – Review & editing; **Yong-feng LI:** Resources, Software; **Heng-rui HU:** Investigation, Software; **He LIU:** Methodology, Software; **Yu-yang GAO:** Methodology, Resources, Software, Supervision, Validation, Visualization; **Zhi-hua DONG:** Funding acquisition, Investigation, Methodology, Project administration, Resources, Software, Supervision, Validation, Visualization, Writing – Original draft, Writing – Review & editing; **Bin JIANG:** Funding acquisition, Investigation, Methodology, Project administration, Resources, Software, Supervision, Validation, Visualization, Writing – Original draft, Writing – Review & editing; **Fu-sheng PAN:** Funding acquisition, Project administration, Supervision.

## Declaration of competing interest

The authors declare that they have no known competing financial interests or personal relationships that could have appeared to influence the work reported in this paper.

## Acknowledgments

This work was financially supported by the National Key Research and Development Program of China (No. 2021YFB3701000), the National Natural Science Foundation of China (Nos. 52471118, 52101125, U2037601, and U21A2048), and Young Elite Scientists Sponsorship Program by CAST, China (No. 2022QNRC001).

## References

[1] WANG G G, WEILER J P. Recent developments in high-pressure die-cast magnesium alloys for automotive and future applications [J]. Journal of Magnesium and Alloys, 2023, 11: 78−87.

[2] SHI Feng-jian, PIAO Nan-ying, WANG Ji-heng, TAN Hao-tian, GUO Yu-hang, YANG Fei, CHEN Shu-jin, LU Sheng, WANG Ze-xin. Tailoring good combinations between strength and ductility in novel Mg−5Sn−2Al−1Zn alloy via different hot extrusion processes [J]. Transactions of Nonferrous Metals Society of China, 2024, 34: 2120−2137.

[3] FAN Yu-tian, LU Li-wei, LIU Jian-bo, MA Min, HUANG Wei-ying, WU Rui-zhi. Effect of deformation temperature on microstructure and texture of AZ31 magnesium alloy processed by new plastic deformation method [J]. Transactions of Nonferrous Metals Society of China, 2024, 34: 2138−2152.

[4] XU Jian, ZHENG Jie, LIU Wan-er, HUANG You-wang, YAN Zhao-ming, ZHANG Zhi-min, WANG Qiang, XUE Yong. Recrystallization behavior and strengthening mechanism of extruded Mg−Gd−Y−Zn−Zr alloy with different pre-aged states [J]. Transactions of Nonferrous Metals Society of China, 2024, 34: 480−503.

[5] HUANG Yu-chuan, ZHANG Quan-da, OUYANG Si-jie, SUN Fu-zhen, SUN Jia-wei, LI Hui-yu, WU Guo-hua, CHEN Pei-jun, LIU Wen-cai. Effects of Zn and Gd contents and their ratios on microstructure and mechanical properties of as-cast and as-extruded Mg−8Li alloys [J]. Transactions of Nonferrous Metals Society of China, 2024, 34: 798−811.

[6] LIU Zhan, NIE Jin-feng, ZHAO Yong-hao. Effect of deformation processing on microstructure evolution and mechanical properties of Mg−Li alloys: A review [J]. Transactions of Nonferrous Metals Society of China, 2024, 34: 1−25.

[7] LIU Qiang, WANG Wen, PENG Pai, ZHANG Ting, HAN Peng, GUAN Xiao-hu, WANG Zhi, QIAO Ke, CAI Jun, WANG Kuai-she. Microstructure evolution and strengthening mechanism of friction stir welded joint of 20 mm-thick AZ31 magnesium alloy [J]. Transactions of Nonferrous Metals Society of China, 2023, 33: 3295−3308.

[8] SONG Jiang-feng, CHEN Jing, XIONG Xiao-ming, PENG Xiao-dong, CHEN Dao-lun, PAN Fu-sheng. Research advances of magnesium and magnesium alloys worldwide in 2021 [J]. Journal of Magnesium and Alloys, 2022, 10: 863−898.

[9] CHEN Han, HU Zhang, HAN Yu-xiang, CHEN Tao, LIU Chu-ming, CHEN Zhi-yong. Microstructure and mechanical properties of Mg−Gd−Y−Zn−Zr alloy plates with different initial textures after hot rolling [J]. Transactions of Nonferrous Metals Society of China, 2024, 34: 1804−1816.

[10] PAN Fu-sheng, YANG Ming-bo, CHEN Xian-hua. A review on casting magnesium alloys: Modification of commercial alloys and development of new alloys [J]. Journal of

Materials Science & Technology, 2016, 32: 1211−1221.

[11] JIANG Bin, DONG Zhi-hua, ZHANG Ang, SONG Jiang-feng, PAN Fu-sheng. Recent advances in micro-alloyed wrought magnesium alloys: Theory and design [J]. Transactions of Nonferrous Metals Society of China, 2022, 32: 1741−1780.

[12] CHEN Wan-tong, YANG Jing-yu, YU Wen-bo, SU Yi-shi, ZHANG Ang, MA Chao-sheng, MA Yi-hu. One developed finite element model used in nano-layered flaky $Ti_2AlC$ MAX ceramic particles reinforced magnesium composite [J]. Journal of Magnesium and Alloys, 2024, 12: 4219−4228.

[13] MA Chao-sheng, YU Wen-bo, PI Xu-feng, GUITTON A. Study of Mg−Al−Ca magnesium alloy ameliorated with designed $Al_8Mn_4Gd$ phase [J]. Journal of Magnesium and Alloys, 2020, 8: 1084−1089.

[14] QIU Cheng-liang, LIU Shu-hong, HUANG Jin-hui, DU Yong. Phase equilibria and solidification behavior of Mg−Al−Gd casting alloys [J]. Transactions of Nonferrous Metals Society of China, 2024, 34: 1091−1109.

[15] KHALAJZADEH V, D.CARLSON Kent, G.BACKMAN D, BECKERMANN C. A pore-centric model for combined shrinkage and gas porosity in alloy solidification [J]. Metallurgical and Materials Transactions A, 2017, 418A: 1797−1816.

[16] ZHOU Bo, MENG De-hao, WU Di, TANG Jian-fei, CHEN Rong-shi, LI Pei-jie, HAN En-hou. Characterization of porosity and its effect on the tensile properties of Mg−6Gd−3Y−0.5Zr alloy [J]. Materials Characterization, 2019, 152: 204−212.

[17] LI Xiao-bo, XIONG Shou-mei, GUO Zhi-peng. On the porosity induced by externally solidified crystals in high-pressure die-cast of AM60B alloy and its effect on crack initiation and propagation [J]. Materials Science and Engineering A, 2015, 633: 35−41.

[18] LI Xiao-bo, XIONG Shou-mei, GUO Zhi-peng. Correlation between porosity and fracture mechanism in high pressure die casting of AM60B alloy [J]. Journal of Materials Science & Technology, 2016, 32: 54−61.

[19] JIANG Jia-hao, GENG Xue, ZHANG Xiao-bo. Stress corrosion cracking of magnesium alloys: A review [J]. Journal of Magnesium and Alloys, 2023, 11: 1906−1930.

[20] WU Meng-wu, HOU Ying-ying, HUA Lin, MA Hui-juan, LI Xiao-bo, XIONG Shou-mei. On the deformation behavior of heterogeneous microstructure and its effect on the mechanical properties of die cast AZ91D magnesium alloy [J]. Journal of Magnesium and Alloys, 2022, 10: 1981−1993.

[21] LI Zi-xin, LI De-jiang, ZHOU Wen-ke, HU Bo, ZHAO Xing-feng, WANG Jing-ya, QIN Ming, XU Jiang-kun, ZENG Xiao-qin. Characterization on the formation of porosity and tensile properties prediction in die casting Mg alloys [J]. Journal of Magnesium and Alloys, 2022, 10: 1857−1867.

[22] LEE C D. Tensile properties of high-pressure die-cast AM60 and AZ91 magnesium alloys on microporosity variation [J]. Journal of Materials Science, 2007, 42: 10032−10039.

[23] LEE C D, SHIN K S. Effect of microporosity on the tensile properties of AZ91 magnesium alloy [J]. Acta Materialia, 2007, 55: 4293−4303.

[24] ZHOU Bo, WU Di, CHEN Rong-shi, HAN En-hou. Enhanced tensile properties in a Mg−6Gd−3Y−0.5Zr alloy due to hot isostatic pressing (HIP) [J]. Journal of Materials Science & Technology, 2019, 35: 1860−1868.

[25] MA Chao-sheng, YU Wen-bo, ZHANG Tong-tong, ZHANG Zhi-hua, MA Yi-hu, XIONG Shou-mei. The effect of slow shot speed and casting pressure on the 3D microstructure of high pressure die casting AE44 magnesium alloy [J]. Journal of Magnesium and Alloys, 2023, 11: 753−761.

[26] LEE S, GOKHALE A M., PATEL G R, EVANS M. Effect of process parameters on porosity distributions in high-pressure die-cast AM50 Mg-alloy [J]. Materials Science and Engineering A, 2006, 427: 99−111.

[27] MI Guo-fa, LIU Xiang-yu, WANG Kuang-fei, FU Heng-zhi. Numerical simulation of low pressure die-casting aluminum wheel [J]. China Foundry, 2009, 6: 48−52.

[28] ZHANG Nan-nan, LEI Chuan, LIU Tian-wen, CAI Hui-sheng, ZHANG Jian-rong, WANG Qu-dong. Parameter optimization of Al−5Mg−3Zn−1Cu basin-shaped centrifugal casting: simulation and experimental verification [J]. International Journal of Metalcasting, 2023, 17: 900−909.

[29] LEE S, HAN D, KANG S, KIM N. Method of predicting shrinkage defects and deriving process conditions in HPDC (High−Pressure Die-Casting) for electric vehicle motor housings [J]. International Journal of Metalcasting, 2023, 18: 1262−1272.

[30] LI Yuan, LIU Jin-xiang, ZHANG Qiang, HUANG Wei-qing. Casting defects and microstructure distribution characteristics of aluminum alloy cylinder head with complex structure [J]. Materials Today Communications, 2021, 27: 102416.

[31] NIYAMA E, UCHIDA T, MORIKAWA M, SAITO S. A method of shrinkage prediction and its application to steel casting practice [J]. The Journal of Japanese Foundry Engineering Society, 1982, 54: 12. (in Japanese)

[32] CARLSON K D, BECKERMANN C. Prediction of shrinkage pore volume fraction using a dimensionless Niyama Criterion [J]. Metallurgical and Materials Transactions A, 2008, 40A: 163−175.

[33] LI Zi-xin, JING Yu-hai, GUO Hong-min, SUN Xiu-yuan, YU Kun, YU An-shan, JIANG Xing-wang, YANG X J. Study of 3D pores and its relationship with crack initiation factors of aluminum alloy die castings [J]. Metallurgical and Materials Transactions B, 2019, 50: 1204−1212.

[34] ZHANG Yong-fa, TAN Wei, ZHENG Jiang, LI Wen-kai, HUANG Shi-yao, XIA Ya-tong, HAN Wei-jian, JIANG Bin. Quantitative analysis of 3D pore characteristics effect on the ductility of HPDC Al−10Si−0.3Mg alloy through X-ray tomography [J]. Journal of Materials Research and Technology, 2023, 26: 8079−8096.

[35] ZHANG Yong-fa, ZHENG Jiang, XIA Ya-tong, SHOU Hao-ge, TAN Wei, HAN Wei-jian, LIU Qing. Porosity quantification for ductility prediction in high pressure die casting AM60 alloy using 3D X-ray tomography [J]. Materials Science and Engineering A, 2020, 772: 138781.

[36] KIRKBY M J. The fractal geometry of nature [J]. Earth Surface Processes and Landforms, 1983, 8: 406−407.

[37] MANDELBROT B. How long is the coast of Britain? Statistical self-similarity and fractional dimension [J]. Science, 1967, 156: 636−638.

[38] WANG Wei-ling, LUO Sen, ZHU Miao-yong. Dendritic

growth of high carbon iron-based alloy under constrained melt flow [J]. Computational Materials Science, 2014, 95: 136−148.
[39] CHANG Q, CHEN Dao-lun, RU Hong-qiang, YUE X, YU Liang. ZHANG Cui-ping, Three-dimensional fractal analysis of fracture surfaces in titanium-iron particulate reinforced hydroxyapatite composites: Relationship between fracture toughness and fractal dimension [J]. Journal of Materials Science, 2011, 46: 6118−6123.
[40] KOBAYASHI S, MARUYAMA T, TSUREKAWA S, WATANABE T. Grain boundary engineering based on fractal analysis for control of segregation-induced intergranular brittle fracture in polycrystalline nickel [J]. Acta Materialia, 2012, 60: 6200−6212.
[41] SU Hui, YAN Zhen-qi. Fractal analyses of martensitic transformations [J]. Materials Letters, 1992, 13: 102−104.
[42] HOU Zi-bing, CAO Jiang-hai, CHANG Yi, WANG W, CHEN H. Morphology characteristics of carbon segregation in die steel billet by ESR based on fractal dimension [J]. Acta Metallurgica Sinica, 2017, 53: 769−777. (in Chinese)
[43] YANG Ai-min, XIONG Yu-hua, LIU Lin. Fractal characteristics of dendrite and cellular structure in nickel-based superalloy at intermediate cooling rate [J]. Science and Technology of Advanced Materials, 2001, 2: 101−103.
[44] ISHIDA H, NATSUME Y, OHSASA K. Characterization of dendrite morphology for evaluating interdendritic fluidity based on phase-field simulation [J]. ISIJ International, 2009, 49: 37−43.
[45] CAO Jiang-hai, HOU Zi-bing, GUO Dong-wei, GUO Zhong-ao, TANG Ping. Morphology characteristics of solidification structure in high-carbon steel billet based on fractal theory [J]. Journal of Materials Science, 2019, 54: 12851−12862.
[46] HOU Zi, JIANG Fang, CHENG Guo-guang. Solidification structure and compactness degree of central equiaxed grain zone in continuous casting billet using cellular automaton-finite element method [J]. ISIJ International, 2012, 52: 1301−1309.
[47] QIU Yi, LI Ying-ju, FENG Xiao-hui, ZHANG Ang, YANG Yuan-sheng. Numerical simulation of microstructure evolution in molten pool of nickel-based superalloy during selective laser melting [J]. Transactions of Nonferrous Metals Society of China, 2024, 34: 560−575.
[48] ZHOU Bo, WU Di, CHEN Rong-shi, HAN En-Hou. Prediction of shrinkage microporosity in gravity-cast and low-pressure sand-cast Mg−6Gd−3Y−0.5Zr magnesium alloys [J]. Advanced Engineering Materials, 2019, 21: 1900755.
[49] KHAJEH E, MAIJER D M. Physical and numerical characterization of the near-eutectic permeability of aluminum–copper alloys [J]. Acta Materialia, 2010, 58: 6334−6344.

# Mg−12Al 镁合金中缩松缺陷的三维形貌特征及其与合金显微组织的关系

李闯名[1,2,3]，张 昂[1,2,3]，李永锋[1,2,3]，胡亨锐[1,2,3]，
刘 和[1,2,3]，高瑜阳[1,2,3]，董志华[1,2,3]，蒋 斌[1,2,3]，潘复生[1,3]

1. 重庆大学 国家镁材料工程技术研究中心，重庆 400044；
2. 重庆大学 高端装备铸造技术全国重点实验室，重庆 400044；
3. 重庆大学 材料科学与工程学院，重庆 400044

**摘 要**：探讨了缩松对 Mg−12Al 合金显微组织特征的依赖关系，分析了不同冷却速率下缩松的分布、形态、尺寸和数量密度，并从温度条件、补缩通道特征和补缩能力等方面讨论了缩松与显微组织特征之间的关系；此外，通过引入渗透率量化了残余液相在固相骨架中的补缩行为。结果表明，固相骨架特征与缩松的形貌特征之间存在很强的相关性，渗透率的增加对应缩松数量密度的下降。通过控制显微组织特征，旨在为减少缩松提供更全面的理解。

**关键词**：Mg−12Al 合金；缩松缺陷；凝固；显微组织特征；形貌特征

**(Edited by Bing YANG)**